Quantum simulation of pairing Hamiltonians with nearest-neighbor-interacting qubits

Zhixin Wang,[1] Xiu Gu,[1,2] Lian-Ao Wu,[3,4] and Yu-xi Liu[1,2,5,*]

[1]*Department of Microelectronics and Nanoelectronics, Tsinghua University, Beijing 100084, China*

[2]*Institute of Microelectronics, Tsinghua University, Beijing 100084, China*

[3]*Ikerbasque, Basque Foundation for Science, 48011 Bilbao, Spain*

[4]*Department of Theoretical Physics and History of Science, The Basque Country University (UPV/EHU), P.O. Box 644, 48080 Bilbao, Spain*

[5]*Tsinghua National Laboratory for Information Science and Technology (TNList), Beijing 100084, China*

(Received 19 November 2014; revised manuscript received 10 October 2015; published 2 June 2016)

Although a universal quantum computer is still far from reach, the tremendous advances in controllable quantum devices, in particular with solid-state systems, make it possible to physically implement "quantum simulators." Quantum simulators are physical setups able to simulate other quantum systems efficiently that are intractable on classical computers. Based on solid-state qubit systems with various types of nearest-neighbor interactions, we propose a complete set of algorithms for simulating pairing Hamiltonians. The fidelity of the target states corresponding to each algorithm is numerically studied. We also compare algorithms designed for different types of experimentally available Hamiltonians and analyze their complexity. Furthermore, we design a measurement scheme to extract energy spectra from the simulators. Our simulation algorithms might be feasible with state-of-the-art technology in solid-state quantum devices.

DOI: 10.1103/PhysRevA.93.062301

I. INTRODUCTION

Classical computers fail to efficiently simulate quantum systems with complex many-body interactions due to the exponential growth of variables for characterizing these systems [1–4]. For instance, 2^N parameters are required for the complete description of a quantum system composed of N entangled spin-1/2 particles. In the 1980s, quantum simulation was proposed to solve such an exponential explosion problem using a controllable quantum system [5]. In 1996, it was shown that a quantum computer containing only few-particle interactions can be used to efficiently simulate many-body quantum Hamiltonians [6]. Quantum simulators are classified into analog and digital ones [1]. An analog quantum simulator is a controllable quantum system that can efficiently mimic the time evolution of other target quantum systems [7], while a digital quantum simulator normally imitates the time evolution of the target system through the implementation of a series of elementary quantum gates [8]. Practically, these two approaches are often combined. A simulation task can be completed through the free evolution of quantum simulators combined with external logic gates at given time instants. Quantum simulators containing tens of qubits are practically useful to carry out classically intractable tasks, while the number of qubits required for practical quantum computing is much larger [1]. Therefore, in comparison with universal quantum computing, quantum simulation is more feasible in the near future, and the simulation algorithms for certain tasks using existing Hamiltonians are strongly desired.

Quantum simulation has attracted extensive attentions (see, e.g., global reviews [1–4] and specialized reviews [9–17]). It can be applied to solve problems in condensed-matter physics (see, e.g., Refs. [7,18]), high-energy physics (see, e.g., Refs. [19,20]), cosmology (see, e.g., Refs. [21,22]), and quantum chemistry (see, e.g., Refs. [12,13,23,24]) with the aim of quantum information processing [25–29]. The latest quantum simulation proposals with respect to many-body problems [30,31] include simulating Heisenberg spin chains with photon-coupled microcavities [32], Cooper pairing with photons [33], correlated-hopping models with ultracold fermionic atoms in optical lattices [34], interacting fermion lattice models [35], and the Holstein model [36] in trapped ions. Quantum simulators using trapped ions [8,15,37,38], cold atoms [14,39], and photons [16] have already been experimentally demonstrated to some extent.

Pairing Hamiltonians, for example, BCS theory in conventional superconductors, feature long-range many-body interactions, which are generally intractable on classical computers. Nevertheless, large-scale numerical calculations based on pairing Hamiltonians are of great importance, for instance, in condensed-matter physics, ultrasmall metallic grains, nuclear physics, and other many-body Hamiltonian systems [40]. To tackle this problem, a polynomial-time quantum algorithm based on nuclear magnetic resonance (NMR) quantum computing was proposed [40] and has been demonstrated experimentally [41,42]. Despite experimental progress on NMR quantum simulators [43,44], liquid NMR has several constrains that make a NMR quantum computer not scalable [45]. Therefore, the large-scale implementation of the NMR-based quantum algorithm is unlikely with the state-of-the-art technology.

In contrast to NMR systems, superconducting quantum circuits have been witnessed in past decades [45–49]. Based on nearest-neighbor coupled superconducting qubits, single-qubit and two-qubit gates with fidelity at the threshold of fault-tolerant quantum computing have been realized recently [50]. The unique flexibility in design and fabrication of superconducting circuits enables the tunability in extensive Hamiltonian parameter ranges. Moreover, the techniques for scaling up are compatible with modern integrated circuits. Both of the above aspects are significant advantages for superconducting quantum circuits to serve as practical quantum simulators [17,51,52]. Many approaches have recently been proposed

*yuxiliu@mail.tsinghua.edu.cn

for simulating dynamical gauge fields [53], Heisenberg and frustrated Ising spin models [54], topological Majorana bound states [55], and quantum phase transitions [56] using superconducting quantum circuits. Also, the research on other solid-state quantum coherence devices, e.g., quantum dots in semiconductors [57] and defect systems [58], has made significant progress recently.

Although various quantum simulation algorithms have been proposed to simulate numerous model Hamiltonians, we find that the pairing Hamiltonian simulation algorithm has not been updated from the NMR system to other ones since 2002. In view of the rapid experimental progress of solid-state quantum computing devices and important applications of the paring Hamiltonian in various many-body systems, it would be of great interest to generalize the quantum simulation algorithm from the NMR system [40] to solid-state ones. Here, we propose a complete set of algorithms and a measurement scheme to simulate pairing models using four representative Hamiltonians, which extensively exist in solid-state quantum systems. The proposed algorithms are suitable for a wide range of controllable solid-state quantum devices, especially superconducting quantum circuits and semiconducting qubit systems.

The remainder of the paper is organized as follows. In Sec. II, we give a brief description of our simulation task and available theoretical Hamiltonians for quantum simulation. General simulation algorithms based on qubits with various types of nearest-neighbor interactions are presented in Sec. III. The fidelity of the algorithms and its variation with various parameters are numerically studied in Sec. IV. The complexity of the algorithms and the parameter dependence is analyzed in Sec. V. We have also designed an effective measurement scheme based on the entanglement of a single qubit in the simulator and an ancillary qubit in Sec. VI, through which crucial information in the energy spectrum could be extracted. We finally summarize our results in Sec. VII.

II. PRELIMINARIES

For the completeness of this paper, first, we briefly review pairing Hamiltonians and outline our simulation tasks.

A. Pairing Hamiltonians and qubit representation

The general BCS pairing Hamiltonian is extensively used in condensed-matter physics and nuclear physics and has the form

$$H_{\mathrm{BCS}} = \sum_{m=1}^{N} \frac{\epsilon_m}{2}\left(n_m^F + n_{-m}^F\right) + \sum_{l=1}^{N}\sum_{m=1}^{N} V_{ml} c_m^\dagger c_{-m}^\dagger c_{-l} c_l, \quad (1)$$

where $c_{\pm m}^\dagger$ and $c_{\pm l}$ are fermionic creation and annihilation operators and $n_{\pm m}^F = c_{\pm m}^\dagger c_{\pm m}$ are fermionic number operators. As has been analyzed (see, for example, Ref. [40]), the BCS pairing Hamiltonian made by fermionic pair operators can be mapped onto qubit operators σ_m^x, σ_m^y, and σ_m^z through the transformation $\{\sigma_m^x,\sigma_m^y,\sigma_m^z\} = \{c_m^\dagger c_{-m}^\dagger + c_{-m}c_m, ic_{-m}c_m - ic_m^\dagger c_{-m}^\dagger, n_m^F + n_{-m}^F - 1\}$. With the mapping, we can rewrite the Hamiltonian in Eq. (1) as

$$H_p = \sum_{m=1}^{N} \frac{\varepsilon_m}{2}\sigma_m^z + \sum_{m<l} \frac{V_{ml}}{2}\left(\sigma_m^x\sigma_l^x + \sigma_m^y\sigma_l^y\right), \quad (2)$$

with $\varepsilon_m = \epsilon_m + V_{mm}$.

B. Qubits with Nearest-Neighbor Coupling

Solid-state qubits can be coupled through various types of interactions. For instance, superconducting qubits can be coupled to their nearest neighbors through capacitances [59], inductances [60], or Josephson junctions [61]. Different interaction models [62] resulting from different coupling schemes can be classified into four categories of commonly used interaction Hamiltonians: longitudinal Ising types [63–65], transverse Ising types [66–68], XY types [69–71], and Heisenberg types [72–76]. These four different types of nearest-neighbor Hamiltonians can be unified as

$$H = H_0 + H_I, \quad (3)$$

with H_0 denoting the single-qubit Hamiltonian

$$H_0 = \sum_{l=1}^{N} \frac{1}{2}\omega_l \sigma_l^z \quad (4)$$

and H_I denoting the interaction Hamiltonian

$$H_I = \sum_{l=1}^{N-1}\left(J_l^x\sigma_l^x\sigma_{l+1}^x + J_l^y\sigma_l^y\sigma_{l+1}^y + J_l^z\sigma_l^z\sigma_{l+1}^z\right). \quad (5)$$

Here, $\sigma_l^x,\sigma_l^y,\sigma_l^z$ are Pauli matrices in the basis of σ_l^z, and l denotes the lth qubit. Parameters J_l ($l = 1,\ldots,N-1$) denote the coupling strength between the lth and $(l+1)$th qubits. Hereafter, we assume $\hbar = 1$.

Each of these four types of Hamiltonians is a special case of Eq. (3) with parameters being properly chosen. The Hamiltonian (3) can be thus reduced to (i) the longitudinal Ising Hamiltonian for parameters $J_l^x = J_l^y = 0$ and $J_l^z = J_l$, (ii) the transverse Ising Hamiltonian for parameters $J_l^y = J_l^z = 0$ and $J_l^x = J_l$, (iii) the XY Hamiltonian for parameters $J_l^z = 0$ and $J_l^x = J_l^y = J_l$, and (iv) the Heisenberg Hamiltonian for parameters $J_l^x = J_l^x = J_l^y = J_l$. For clarity, we summarize them in Table I.

Assuming that qubit systems with nearest-neighbor couplings in Eq. (3) are available experimentally, we can hence use them to simulate dynamical behaviors of pairing Hamiltonians in Eq. (2) with the help of single-qubit operations. These operations will be done by applying external fields $F = \sum_{l=1}^{N}(f_l^x\sigma_l^x + f_l^y\sigma_l^y + f_l^z\sigma_l^z)$ to individual qubits. It is clear

TABLE I. Summary of various interaction Hamiltonians in solid-state systems with single-qubit Hamiltonians $H_0 = \sum_{l=1}^{N}(\omega_l\sigma_l^z/2)$. Note that $J_l^x = J_l^y = J_l$ for the Heisenberg model.

Interaction type	Interaction Hamiltonian
Longitudinal Ising model	$H_{\mathrm{Ising,L}} = H_0 + \sum_{l=1}^{N-1} J_l\sigma_l^z\sigma_{l+1}^z$
Transverse Ising model	$H_{\mathrm{Ising,T}} = H_0 + \sum_{l=1}^{N-1} J_l\sigma_l^x\sigma_{l+1}^x$
XY model	$H_{XY} = H_0 + \sum_{i=x,y}\sum_{l=1}^{N-1} J_l\sigma_l^i\sigma_{l+1}^i$
Heisenberg model	$H_{\mathrm{H}} = H_0 + \sum_{i=x,y,z}\sum_{l=1}^{N-1} J_l^i\sigma_l^i\sigma_{l+1}^i$

that the pairing models in Eq. (2) do not share the same form of Hamiltonians in Eq. (3). Therefore, it is necessary to design algorithms to simulate these pairing Hamiltonians using the four types of interaction Hamiltonians mentioned above.

C. Quantum simulations

Our goal is to simulate the BCS-type pairing Hamiltonian in Eq. (2), which can be rewritten as

$$H_p = H_{p0} + H_{pI}, \tag{6}$$

where $H_{p0} = \sum_{m=1}^{N} \varepsilon_m \sigma_m^z/2$ is the single-qubit Hamiltonian and $H_{pI} = \sum_{l>m}^{N} V_{ml}(\sigma_m^x \sigma_l^x + \sigma_m^y \sigma_l^y)/2$ is the interaction Hamiltonian.

We now come to simulate parameters ε_m $(m = 1 \ldots N)$ and V_{ml} $(m,l = 1 \ldots N, m < l)$ in Eq. (6) with each of the Hamiltonians in Table I using the decoupling and recoupling techniques in Ref. [77]. The single-qubit terms $\varepsilon_m \sigma_m^z/2$ $(m = 1, \ldots, N)$ and two-qubit interaction Hamiltonian terms $V_{ml}(\sigma_m^x \sigma_l^x + \sigma_m^y \sigma_l^y)/2$ $(l,m = 1, \ldots, N, l < m)$ will be simulated separately through dynamical evolution. Special care must be taken when the separated terms are all put together using Trotter's formula [78,79] since operators σ_m^x, σ_m^y, and σ_m^z do not commute with each other. Another challenge is to simulate long-range interaction terms in H_p through simulators containing only nearest-neighbor interactions. Therefore, methods for extending the range of interaction must be properly designed.

We note that the tunability of parameters ω_l $(l = 1, \ldots, N)$ and J_l^i $(i = x,y,z; l = 1, \ldots, N-1)$ affects the efficiency of the algorithms. Algorithms for simulators with constant parameters presented in the following section are often more complex. Simplification is allowed if some of the parameters are tunable during the simulation process. A comparison of fidelity and complexity between simulators with constant and tunable coupling parameters will be given in Secs. IV and V.

III. SIMULATION ALGORITHMS

In this section, we give a detailed discussion of how to simulate a pairing Hamiltonian using Ising-type, XY-type, or Heisenberg-type interaction Hamiltonians as listed in Table I.

A. Algorithm for simulators with the longitudinal Ising Hamiltonian

We first study an algorithm to simulate pairing Hamiltonians using the longitudinal Ising Hamiltonian. The simulation algorithm needs two steps [40]. The first step is to simulate H_{p0}, and the second one is to mimic H_{pI}. We then combine H_{p0} and H_{pI} to obtain the complete pairing Hamiltonian. The detailed description of these steps is as given below.

1. *Simulation algorithm for individual terms H_{p0}*

We now use the simulators with longitudinal Ising-type interaction $H_{\mathrm{Ising,L}}$ in Table I to simulate H_{p0}. The operator

$$U_{\mathrm{Ising,L}}(\tau) = e^{-i\tau H_{\mathrm{Ising,L}}} \tag{7}$$

denotes the time-evolution operator of the quantum simulator. Let us consider the time-evolution operator $U_l^z(\tau) = \exp(-i\tau\omega_l\sigma_l^z/2)$ of the lth qubit. Using a method similar to that shown in Ref. [40], we show that $U_l^z(\tau)$ can be given as (see the Appendix for detailed derivations)

$$\begin{aligned} U_l^z(\tau) &= \left(\bigotimes_{j''\neq l} e^{i\frac{\pi}{2}\sigma_{j''}^x}\right) U_{\mathrm{Ising,L}}\left(\frac{\tau}{4}\right)\left(\bigotimes_{j'} e^{i\frac{\pi}{2}\sigma_{j'}^x}\right) U_{\mathrm{Ising,L}}\left(\frac{\tau}{4}\right) \\ &\times \left(\bigotimes_{j''\neq l} e^{-i\frac{\pi}{2}\sigma_{j''}^x}\right) U_{\mathrm{Ising,L}}\left(\frac{\tau}{4}\right)\left(\bigotimes_{j'} e^{-i\frac{\pi}{2}\sigma_{j'}^x}\right) U_{\mathrm{Ising,L}}\left(\frac{\tau}{4}\right) \end{aligned} \tag{8}$$

using $U_{\mathrm{Ising,L}}(\tau/4)$. Here, j' and j'' denote the j'th and the j''th qubits in the simulator. j' is an even (odd) number, and j'' is an odd (even) number if l is an odd (even) number, where $j'' \neq l$. The detailed quantum circuits to realize single-qubit operation $U_l^z(\tau)$ in Eq. (8) are shown in Fig. 1. We note that all following logic operations and corresponding circuits are derived and given by using a method similar to that for Eq. (8) and correspond to Fig. 1.

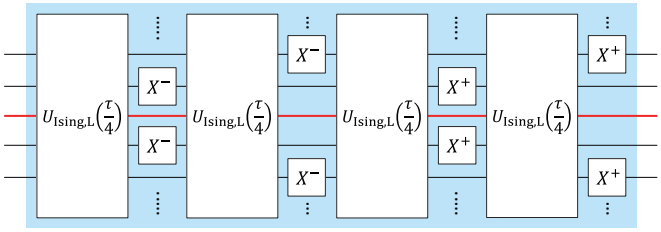

FIG. 1. The quantum circuit to realize $U_l^z(\tau)$ from $U_{\mathrm{Ising,L}}$. The thick red line stands for the lth qubit in the system, whose individual evolution term is going to be extracted through this step. Black dots on both sides stand for the periodic extension of the logic gates to the rest of the system in the given direction. Here, the period is 2. $X^{\pm}$ stand for external gates $e^{\pm i\frac{\pi}{2}\sigma^x}$.

For a given $U_l^z(\tau)$, we can extract the time evolution $H_{\mathrm{Ising,L}}$ of each single qubit and then simulate H_{p0} through the circuit $e^{-itH_{p0}} = \bigotimes_{m=1}^{N} U_m^z(\tau)$, with $\tau = \varepsilon_m t/\omega_m$. Therefore, an individual $U_l^z(\tau)$ is the building block when simulating H_{p0}. In the following sections we will show that $U_l^z(\tau)$ can be simulated on simulators with other types of interactions.

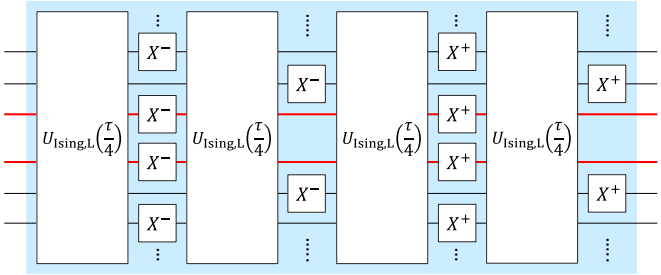

FIG. 2. The quantum circuit for simulating $U_{l,l+1}^{zz}(\tau)$ directly from $U_{\mathrm{Ising,L}}(\tau)$. The thick red lines stand for the lth and the $(l+1)$th qubits in the system. For the extension represented by the black dots on both sides, the period is 2.

2. *Simulation algorithm for interactions H_{pI} and H_p*

Before simulating H_{pI} of the pairing Hamiltonian in Eq. (6) we first consider a time-evolution operator $U^{zz}_{l,m}(\tau) = \exp(-i\tau J_l \sigma^z_l \sigma^z_m)$. If the simulator has longitudinal Ising nearest-neighbor couplings, $U^{zz}_{l,l+1}(\tau)$ can be directly obtained from $U_{\mathrm{Ising,L}}(\tau)$ through the circuit as in Fig. 2, which can be expressed as

$$\begin{aligned} U^{zz}_{l,l+1}(\tau) = &\left(\bigotimes_{j'<l} e^{i\frac{\pi}{2}\sigma^x_{j'}}\right)\left(\bigotimes_{j''>l+1} e^{i\frac{\pi}{2}\sigma^x_{j''}}\right) U_{\mathrm{Ising,L}}\left(\frac{\tau}{4}\right) \\ &\times \left(\bigotimes_{j''\leqslant l} e^{i\frac{\pi}{2}\sigma^x_{j''}}\right)\left(\bigotimes_{j'\geqslant l+1} e^{i\frac{\pi}{2}\sigma^x_{j'}}\right) U_{\mathrm{Ising,L}}\left(\frac{\tau}{4}\right) \\ &\times \left(\bigotimes_{j'<l} e^{-i\frac{\pi}{2}\sigma^x_{j'}}\right)\left(\bigotimes_{j''>l+1} e^{-i\frac{\pi}{2}\sigma^x_{j''}}\right) U_{\mathrm{Ising,L}}\left(\frac{\tau}{4}\right) \\ &\times \left(\bigotimes_{j''\leqslant l} e^{-i\frac{\pi}{2}\sigma^x_{j''}}\right)\left(\bigotimes_{j'\geqslant l+1} e^{-i\frac{\pi}{2}\sigma^x_{j'}}\right) U_{\mathrm{Ising,L}}\left(\frac{\tau}{4}\right). \end{aligned} \tag{9}$$

Here, j' and j'' for the j'th and the j''th qubits in the simulator satisfy the condition that j' is even (odd) and j'' is odd (even) if l is odd (even), where j'' may equal to l. Using the time-evolution operator $U^{zz}_{l,l+1}(\tau)$ in Eq. (9) and single-qubit operations, we have

$$\begin{aligned} U^{xx+yy}_{l,l+1}(\tau) = \exp(-i\tau H^{xy}_l) = e^{i\frac{\pi}{4}Y_{l,l+1}} U^{zz}_{l,l+1}(\tau) e^{-i\frac{\pi}{4}Y_{l,l+1}} \\ \times e^{i\frac{\pi}{4}X_{l,l+1}} U^{zz}_{l,l+1}(\tau) e^{-i\frac{\pi}{4}X_{l,l+1}} + O(J^2\tau^2). \end{aligned} \tag{10}$$

Here, the Hamiltonian H^{xy}_l denotes the interaction between the lth and $(l+1)$th qubits in the xy plane, and

$$H^{xy}_l = J_l\left(\sigma^x_l \sigma^x_{l+1} + \sigma^y_l \sigma^y_{l+1}\right). \tag{11}$$

We hereafter label the sum of Pauli operators of the lth and $(l+1)$th qubits as

$$P_{l,l+1} = \sigma^p_l + \sigma^p_{l+1}, \tag{12}$$

where $P = X, Y, Z$ correspond to $p = x, y, z$, respectively. For instance, $Y_{l,l+1}$ is expressed as $Y_{l,l+1} = \sigma^y_l + \sigma^y_{l+1}$.

With all nearest-neighbor coupling operators $U^{zz}_{l,l+1}(\tau)$ and $U^{xx+yy}_{l,l+1}(\tau)$ being simulated, we can extend the nearest-neighbor interactions to long-range interactions and eventually obtain the total BCS interactions H_{pI} by following the method proposed in Ref. [40]. When H_{p0} and H_{pI} are both available, the total Hamiltonian can be obtained by Trotter's formula $e^{-itH_p} = e^{-itH_{p0}} e^{-itH_{pI}} + O(t^2)$. In comparison with the exponential complexity to carry out the same task on classical computers, ideally, we need only $O(N^4)$ external single-qubit quantum gates to implement the simulation algorithm.

The discussions above show that the simulations of the nearest-neighbor propagators $U^{zz}_{l,l+1}(\tau)$ and $U^{xx+yy}_{l,l+1}(\tau)$ are crucial in the entire simulating process. In the following sections, we will explain that $U^{zz}_{l,l+1}(\tau)$ and $U^{xx+yy}_{l,l+1}(\tau)$ can also be simulated through other types of Hamiltonians.

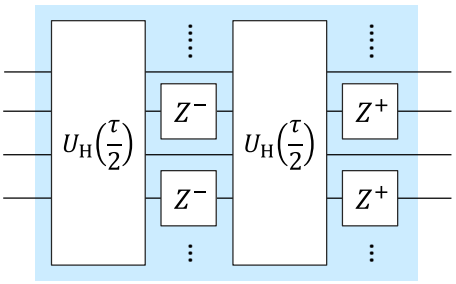

FIG. 3. Quantum circuit to simulate $U_{\mathrm{Ising,L}}(\tau)$ from $U_{\mathrm{H}}(\tau)$. $Z^{\pm}$ stand for external gates $e^{\pm i\frac{\pi}{2}\sigma^z}$. Black dots on both sides stand for the periodic extension of the logic gates starting from any single qubit. Here, the period is two.

B. Algorithm for simulators with Heisenberg nearest-neighbor interaction

1. *Simulation algorithm for H_{p0}*

We now study how to obtain H_{p0} if we have only Heisenberg-type Hamiltonian and rotations around the x direction. Based on Trotter's formula, we can decompose the time-evolution operator with the Heisenberg-type interaction Hamiltonian into

$$\begin{aligned} U_{\mathrm{H}}(\tau) = e^{-i\tau H_{\mathrm{H}}} \approx \exp\left(\sum_{l=1}^{N} \frac{\omega^z_l}{2}\sigma_z\right) \exp\left(-i\tau \sum_{l=1}^{N} H^{zz}_l\right) \\ \times \exp\left(-i\tau \sum_{l=1}^{N-1} H^{xy}_l\right) + O(J^2\tau^2), \end{aligned} \tag{13}$$

with $H^{zz}_l = J_l \sigma^z_l \sigma^z_{l+1}$.

When the quantum simulators possess Heisenberg-type interaction, we can first simulate the longitudinal Ising Hamiltonian using the Heisenberg Hamiltonian and then H_{p0} in terms of the longitudinal Ising Hamiltonian. The latter step has already been solved. Assume that error up to $O(J^2\tau^2)$ is tolerable; we can obtain the longitudinal Ising Hamiltonian through

$$\begin{aligned} U_{\mathrm{Ising,L}}(\tau) \approx \left(\bigotimes_j e^{i\frac{\pi}{2}\sigma^z_{2j}}\right) U_{\mathrm{H}}\left(\frac{\tau}{2}\right) \left(\bigotimes_j e^{-i\frac{\pi}{2}\sigma^z_{2j}}\right) \\ \times U_{\mathrm{H}}\left(\frac{\tau}{2}\right). \end{aligned} \tag{14}$$

Here, $2j$ denotes that the qubits with even indices are rotated $\pm\pi/2$ around the z direction, and the qubits with odd indices remain unchanged. We can also rotate all qubits with odd indices $\pm\pi/2$ around the z axis to obtain the same result. Figure 3 shows the corresponding quantum circuit.

2. *Simulation algorithm for interaction H_{pI}*

We now design the algorithm to simulate the long-range XY interaction terms in the pairing Hamiltonian in Eq. (6) using a quantum simulator with Heisenberg interaction. Let us first consider two time-evolution operators

$$U_{zz}(\tau) = \exp\left(-i\tau \sum_{l=1}^{N-1} J_l \sigma^z_l \sigma^z_{l+1}\right) \tag{15}$$

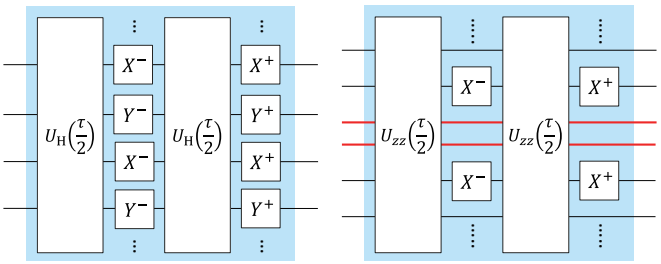

(a) (b)

FIG. 4. The quantum circuits to simulate (a) $U_{zz}(\tau)$ from $U_{\rm H}(\tau)$ and (b) $U^{zz}_{l,l+1}(\tau)$ from $U_{zz}(\tau)$. The thick red lines stand for the lth and the $(l+1)$th qubits in the system, whose interaction is to be extracted through this step. The period for the extension on both sides represented by black dots is 2. $Y^{\pm}$ stand for external gates $e^{\pm i\frac{\pi}{2}\sigma^y}$.

and

$$U^{zz}_{l,m}(\tau) = \exp\big(-i\tau J_l \sigma^z_l \sigma^z_m\big). \tag{16}$$

We note that U_{zz} in Eq. (15) is different from $U_{\rm Ising,\,L}$ in Eq. (7) because $U_{\rm Ising,\,L}$ includes a free evolution of the system. As shown in Fig. 4(a), $U_{zz}(\tau)$ can be simulated through $U_{\rm H}(\tau)$ with error up to order $O(J^2\tau^2)$. Here, $U_{\rm H}(\tau)$ is the time-evolution operator of simulators with Heisenberg interactions,

$$\begin{aligned} U_{zz}(\tau) \approx & \left(\bigotimes_j e^{i\frac{\pi}{2}\sigma^x_{2j}}\right)\left(\bigotimes_j e^{i\frac{\pi}{2}\sigma^y_{2j+1}}\right)U_{\rm H}\Big(\frac{\tau}{2}\Big) \\ & \times\left(\bigotimes_j e^{-i\frac{\pi}{2}\sigma^x_{2j}}\right)\left(\bigotimes_j e^{-i\frac{\pi}{2}\sigma^y_{2j+1}}\right)U_{\rm H}\Big(\frac{\tau}{2}\Big). \end{aligned} \tag{17}$$

Figure 4(b) shows that $U^{zz}_{l,l+1}(\tau)$ can be simulated through $U_{zz}(\tau)$, that is,

$$\begin{aligned} U^{zz}_{l,l+1}(\tau) = & \left(\bigotimes_{j'<l} e^{i\frac{\pi}{2}\sigma^x_{j'}}\right)\left(\bigotimes_{j''>l+1} e^{i\frac{\pi}{2}\sigma^x_{j''}}\right)U_{zz}\Big(\frac{\tau}{2}\Big) \\ & \times\left(\bigotimes_{j'<l} e^{-i\frac{\pi}{2}\sigma^x_{j'}}\right)\left(\bigotimes_{j''>l+1} e^{i\frac{\pi}{2}\sigma^x_{j''}}\right)U_{zz}\Big(\frac{\tau}{2}\Big), \end{aligned} \tag{18}$$

where j' and j'' denote the j'th and j''th qubits in the simulator. Here, j' is even (odd), and j'' is (even) when l is an odd (even) number. If $O(J^2\tau^2)$ is negligibly small, $U^{xx+yy}_{l,l+1}(\tau)$ can be obtained in the same way as it is in Eq. (10).

There is an alternative approach to simulate $U^{xx+yy}_{l,l+1}(\tau)$ through simulators with Heisenberg interactions. We first show how to obtain the operation

$$U_{xx+yy}(\tau) = \exp\left[-i\tau\sum_{l=1}^{N-1} J_l\big(\sigma^x_l\sigma^x_{l+1} + \sigma^y_l\sigma^y_{l+1}\big)\right], \tag{19}$$

which describes the time evolution for the XY model without free Hamiltonians. Figure 5(a) shows that $U_{xx+yy}(\tau)$ can be

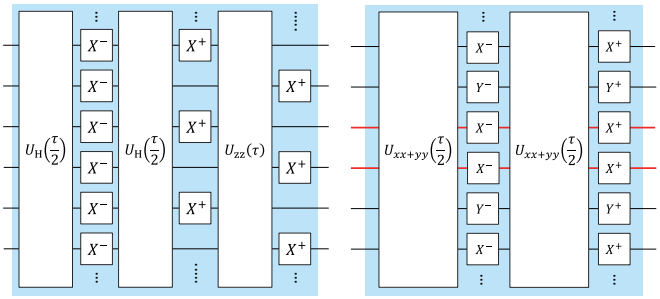

(a) (b)

FIG. 5. The quantum circuits to simulate (a) $U_{xx+yy}(\tau)$ from $U_{\rm H}(\tau)$ and (b) $U^{xx+yy}_{l,l+1}(\tau)$ directly from $U_{xx+yy}(\tau)$. The thick red lines stand for the lth and the $(l+1)$th qubits in the system. Black dots on both sides stand for the periodic extension of the logic gates to the rest of the system in the given direction. In (a), for operators X^- in the left column the period is 1, while for operators X^+ in the middle and right columns the period is 2. In (b), the period is 2.

simulated through $U_{\rm H}(\tau)$, that is,

$$\begin{aligned} U_{xx+yy}(\tau) \approx & \left(\bigotimes_j e^{i\frac{\pi}{2}\sigma^x_{2j}}\right)U_{zz}(\tau)\left(\bigotimes_j e^{i\frac{\pi}{2}\sigma^x_{2j+1}}\right) \\ & \times U_{\rm H}\Big(\frac{\tau}{2}\Big)\left(\bigotimes_j e^{-i\frac{\pi}{2}\sigma^x_j}\right)U_{\rm H}\Big(\frac{\tau}{2}\Big). \end{aligned} \tag{20}$$

Then $U^{xx+yy}_{l,l+1}(\tau)$ can be realized from $U_{xx+yy}(\tau)$ as in Fig. 5(b), which is given as

$$\begin{aligned} U^{xx+yy}_{l,l+1}(\tau) \approx & \left(\bigotimes_{j''\leqslant l} e^{i\frac{\pi}{2}\sigma^x_{j''}}\right)\left(\bigotimes_{j'>l+1} e^{i\frac{\pi}{2}\sigma^x_{j'}}\right) \\ & \times\left(\bigotimes_{j'\leqslant l} e^{i\frac{\pi}{2}\sigma^y_{j'}}\right)\left(\bigotimes_{j''>l} e^{i\frac{\pi}{2}\sigma^x_{j''}}\right)U_{xx+yy}\Big(\frac{\tau}{2}\Big) \\ & \times\left(\bigotimes_{j'\leqslant l} e^{-i\frac{\pi}{2}\sigma^y_{j'}}\right)\left(\bigotimes_{j''>l} e^{-i\frac{\pi}{2}\sigma^x_{j''}}\right) \\ & \times\left(\bigotimes_{j''\leqslant l} e^{-i\frac{\pi}{2}\sigma^x_{j''}}\right)\left(\bigotimes_{j'>l+1} e^{-i\frac{\pi}{2}\sigma^x_{j'}}\right)U_{xx+yy}\Big(\frac{\tau}{2}\Big). \end{aligned} \tag{21}$$

The approximation is valid when $O(J^2\tau^2)$ is negligible. j' is even (odd) while j'' is odd (even) if l is odd (even), where j'' may equal to l.

Furthermore, since the Heisenberg interactions can be converted to the longitudinal Ising Hamiltonians in Eq. (14), after this conversion the simulation can also be done according to the algorithm for simulators with longitudinal Ising Hamiltonians.

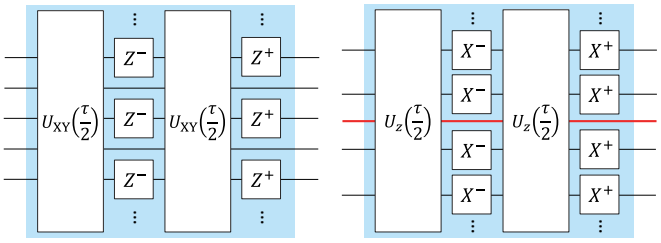

FIG. 6. The quantum circuit for achieving (a) $U_z(\tau)$ from $U_{\rm XY}(\tau)$ and (b) $U_l^z(\tau)$ from $U_z(\tau)$. The thick red line stands for the lth qubit in the system. The period of extension represented by black dots is 2 in (a) and 1 in (b).

C. Algorithm for simulators with the XY nearest-neighbor interaction

1. Simulation algorithm for H_{p0}

If simulators with the XY interaction are available and the transition frequencies of all qubits in the simulators are identical or almost identical, the time-evolution operator is separable; that is, $U_{XY}(\tau)=\exp(-i\tau H_{XY})$ can be expressed as

$$U_{\rm XY}(\tau)=e^{-i\tau H_{\rm XY}}=\exp(-i\tau H_0)\exp\left[-i\tau\sum_{l=1}^{N-1}H_l^{xy}\right]. \tag{22}$$

Here, H_{XY}, H_0, and H_l^{xy} are given in Table I, Eq. (4), and Eq. (11), respectively. Figure 6(a) shows when the Heisenberg Hamiltonian in Fig. 3 is replaced by the XY type Hamiltonian, we can obtain $U_z(\tau)=\exp(-i\tau\sum_{l=1}^{N}\omega_l\sigma_l^z/2)$, which can be expressed as

$$U_z(\tau)=\left(\bigotimes_j e^{i\frac{\pi}{2}\sigma_{2j}^z}\right)U_{\rm XY}\left(\frac{\tau}{2}\right)\left(\bigotimes_j e^{-i\frac{\pi}{2}\sigma_{2j}^z}\right)U_{\rm XY}\left(\frac{\tau}{2}\right). \tag{23}$$

The quantum circuit for $U_l^z(\tau)$ is shown in Fig. 6(b) and can be expressed as

$$U_l^z(\tau)=\left(\bigotimes_{j\neq l} e^{i\frac{\pi}{2}\sigma_j^x}\right)U_z\left(\frac{\tau}{2}\right)\left(\bigotimes_{j\neq l} e^{-i\frac{\pi}{2}\sigma_j^x}\right)U_z\left(\frac{\tau}{2}\right). \tag{24}$$

The single-qubit Hamiltonian H_{p0} can be simulated from $U_l^z(\tau)$ in the same way as those for longitudinal Ising and Heisenberg interactions.

2. Simulation algorithm for interaction H_{pI}

If we use simulators with XY interactions, then $U_{xx+yy}(\tau)$ can be simulated in the following way:

$$U_{xx+yy}(\tau)=\left(\bigotimes_j e^{i\frac{\pi}{2}\sigma_j^x}\right)U_{\rm XY}\left(\frac{\tau}{2}\right)\times\left(\bigotimes_j e^{-i\frac{\pi}{2}\sigma_j^x}\right)U_{\rm XY}\left(\frac{\tau}{2}\right), \tag{25}$$

which is shown in Fig. 7(a).

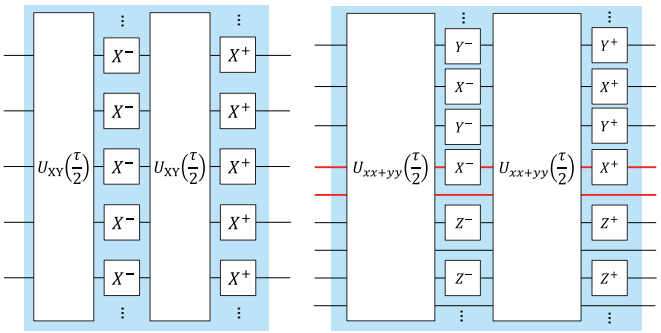

FIG. 7. The quantum circuits for simulating (a) $U_{xx+yy}(\tau)$ from $U_{\rm XY}(\tau)$ and (b) $U_{l,l+1}^{xx}(\tau)$ directly from $U_{xx+yy}(\tau)$. The thick red lines stand for the lth and the $(l+1)$th qubits in the system. Black dots on both sides stand for the periodic extension of the logic gates. In (a) the period is 1, while in (b) the period is 2.

Figure 7(b) shows that we can acquire $U_{l,l+1}^{xx}(\tau)$ from $U_{xx+yy}(\tau)$ in the following way:

$$\begin{aligned}U_{l,l+1}^{xx}(\tau)=&\left(\bigotimes_{j''} e^{i\frac{\pi}{2}\sigma_{j''}^x}\right)\left(\bigotimes_{j'<l} e^{i\frac{\pi}{2}\sigma_{j'}^y}\right)\\&\times\left(\bigotimes_{j'>l+1} e^{i\frac{\pi}{2}\sigma_{j'}^y}\right)U_{xx+yy}\left(\frac{\tau}{2}\right)\\&\times\left(\bigotimes_{j'<l} e^{-i\frac{\pi}{2}\sigma_{j'}^y}\right)\left(\bigotimes_{j'>l+1} e^{-i\frac{\pi}{2}\sigma_{j'}^y}\right)\\&\times\left(\bigotimes_{j''} e^{-i\frac{\pi}{2}\sigma_{j''}^x}\right)U_{xx+yy}\left(\frac{\tau}{2}\right).\end{aligned} \tag{26}$$

Here, j' is even (odd), and j'' is odd (even) when l is an odd (even) number, where j'' may equal to l. We can then obtain $U_{l,l+1}^{zz}(\tau)$ in terms of

$$U_{l,l+1}^{zz}(\tau)=e^{i\frac{\pi}{4}(\sigma_l^y+\sigma_{l+1}^y)}U_{l,l+1}^{xx}(\tau)e^{-i\frac{\pi}{4}(\sigma_l^y+\sigma_{l+1}^y)}. \tag{27}$$

Then $U_{l,l+1}^{xx+yy}(\tau)$ can be simulated using $U_{l,l+1}^{zz}(\tau)$ according to Eq. (10). We note that $U_{l,l+1}^{xx+yy}(\tau)$ can also be directly given through the process

$$\begin{aligned}U_{l,l+1}^{xx+yy}(\tau)=&U_{l,l+1}^{xx}(\tau)e^{i\frac{\pi}{4}(\sigma_l^z+\sigma_{l+1}^z)}U_{l,l+1}^{xx}(\tau)e^{-i\frac{\pi}{4}(\sigma_l^z+\sigma_{l+1}^z)}\\&+O(J^2\tau^2).\end{aligned} \tag{28}$$

Then the interaction Hamiltonian H_{pI} can be finally simulated in the same way as shown in Ref. [40].

D. Algorithm for simulators with the transverse Ising nearest-neighbor interaction

1. Simulation algorithm for individual H_{p0}

In contrast to the above cases, $U_{\rm Ising,T}(\tau)=e^{-i\tau H_{\rm Ising,T}}$ for the Hamiltonian with transverse Ising interactions is not exactly separable. Even so, as shown in Fig. 8(a), $U_z(\tau)$ can be extracted by the same quantum circuit as in Figs. 6(a) and 6(b)

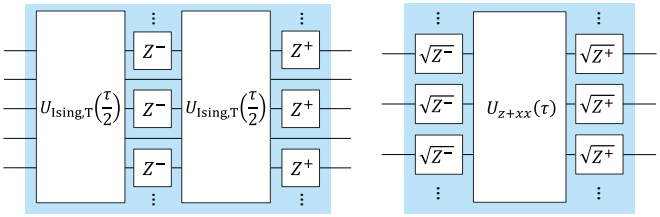

FIG. 8. The quantum circuit for simulating (a) $U_z(\tau)$ from $U_{\mathrm{Ising,T}}$ and (b) $U_{z+yy}(\tau;\omega_1,\ldots,\omega_N)$ from $U_{z+xx}(\tau;\omega_1,\ldots,\omega_N)$. Black dots on both sides stand for the extension of the logic gates with period 1. $\sqrt{Z^{\pm}}$ stand for external gates $e^{\pm i\frac{\pi}{4}\sigma^z}$.

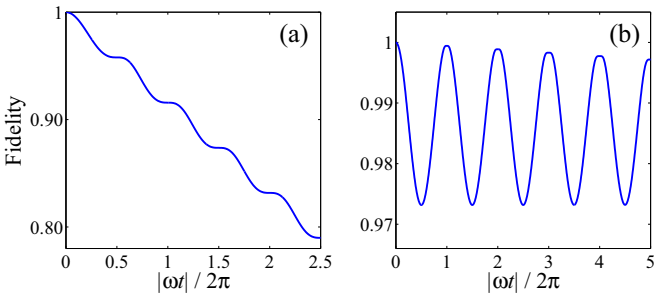

FIG. 9. Digital fidelity of (a) $e^{-i\tau H_{\mathrm{Ising,T}}} \approx \exp(-i\tau\sum_{l=1}^{N}\omega_l\sigma_l^z/2)\exp[-i\tau\sum_{l=1}^{N-1}J_l(\sigma_l^x\sigma_{l+1}^x+\sigma_l^y\sigma_{l+1}^y+\sigma_l^z\sigma_{l+1}^z)]$ and (b) the process shown in Fig. 8(a) for a four-qubit quantum simulator. $\varepsilon_l = 2\times10^{12}$Hz, $\omega_l = 5\times10^9$Hz ($l=1,\ldots,N$), $V_l = -2\times10^8$Hz, and $J_l = 3\times10^7$Hz ($l=1,\ldots,N-1$). The fluctuations on the curves originate from the trigonometric terms in Eq. (33) with period π/ω in (a) and $2\pi/\omega$ in (b).

2. *Simulation algorithm for interaction H_{p1}*

Let us first consider a time-evolution operator

$$U_{z+xx}(\tau) = \exp\left[-i\tau\left(\sum_{l=1}^{N}\frac{\omega_l}{2}\sigma_l^z + \sum_{l=1}^{N-1}J_l\sigma_l^x\sigma_{l+1}^x\right)\right], \quad (29)$$

which is exactly the same as $U_{\mathrm{Ising,T}}(\tau)$ with tunable parameters ω_l ($l=1,\ldots,N$). Similarly, we also consider

$$U_{z+yy}(\tau) = \exp\left[-i\tau\left(\sum_{l=1}^{N}\frac{\omega_l}{2}\sigma_l^z + \sum_{l=1}^{N-1}J_l\sigma_l^y\sigma_{l+1}^y\right)\right]. \quad (30)$$

The operation $U_{z+yy}(\tau)$ can be acquired from $U_{z+xx}(\tau)$ by

$$U_{z+yy}(\tau) = \left(\bigotimes_{j=1}^{N}e^{i\frac{\pi}{4}\sigma_j^z}\right)U_{z+xx}(\tau)\left(\bigotimes_{j=1}^{N}e^{-i\frac{\pi}{4}\sigma_j^z}\right), \quad (31)$$

which is graphically shown in Fig. 8(b). If all qubit resonance frequencies in $U_{z+xx}(\tau)$ are set to be ω and those in $U_{z+yy}(\tau)$ are set to be $-\omega$, we have

$$U_{xx+yy}(\tau) \approx U_{z+xx}(\tau)U_{z+yy}(\tau) \quad (32)$$

up to order $O(J^2\tau^2)$. Here, the negative qubit resonance frequencies mean that inverse external fields are used to flip the sign of $\sum_{l=1}^{N}\omega_l\sigma_l^z/2$. Thus, the simulation using the transverse Ising Hamiltonian is converted to the cases of Heisenberg or XY Hamiltonians as studied before.

IV. NUMERICAL STUDY OF FIDELITY

We now study numerically the error introduced by Trotter's formula, which is typically on the order of $O(J^2t^2)$ or $O(\omega Jt^2)$. Our focus will be the fidelity of the simulated Hamiltonian using the simulation algorithms, although our algorithms can be applied to any system which has the above-mentioned interaction Hamiltonian. However, for concreteness and as an example, the parameters used in following simulation are mainly taken from superconducting quantum devices [17].

In Sec. III, we assumed for generality that all of the algorithms are applicable to simulators with constant coupling strengths and frequencies. However, if simulators with tunable parameters are available, we can not only simplify the simulation process but also reduce digital errors significantly. For instance, $e^{-i\tau H_{\mathrm{Ising,T}}} = \exp(-i\tau\sum_{l=1}^{N}\omega_l\sigma_l^z/2)\exp[-i\tau\sum_{l=1}^{N-1}J_l(\sigma_l^x\sigma_{l+1}^x+\sigma_l^y\sigma_{l+1}^y+\sigma_l^z\sigma_{l+1}^z)]$ does not hold exactly in general. Detailed calculation indicates

$$\begin{aligned}
&\exp\left(-i\tau\sum_{l=1}^{N}\frac{\omega}{2}\sigma_l^z\right)\exp\left(-i\tau\sum_{l=1}^{N-1}J\sigma_l^x\sigma_{l+1}^x\right)\\
&= \exp\left\{-i\tau\left(\sum_{l=1}^{N}\frac{\omega}{2}\sigma_l^z + \sum_{l=1}^{N-1}J\sigma_l^x\sigma_{l+1}^x\right)\right.\\
&\quad + \frac{i\tau}{2}\sum_{l=1}^{N-1}J\left(\sigma_l^x\sigma_{l+1}^x - \sigma_l^y\sigma_{l+1}^y\right)\\
&\quad - \frac{i}{4\omega}\sum_{l=1}^{N-1}J\left(\sigma_l^x\sigma_{l+1}^x - \sigma_l^y\sigma_{l+1}^y\right)\sin(2\omega\tau)\\
&\quad \left. + \frac{i}{4\omega}\sum_{l=1}^{N-1}J\left(\sigma_l^y\sigma_{l+1}^x + \sigma_l^x\sigma_{l+1}^y\right)[\cos(2\omega\tau)-1]\right\},
\end{aligned} \quad (33)$$

where $i\tau\sum_{l=1}^{N-1}J(\sigma_l^x\sigma_{l+1}^x - \sigma_l^y\sigma_{l+1}^y)/2$ is the error that will accumulate during simulation processes. These terms containing $\sin(2\omega\tau)$ and $\cos(2\omega\tau)$ are the origins of the fluctuations of period π/ω on the fidelity curve, as shown in Fig. 9(a). Numerical simulation shows that the fidelity of the circuit in Fig. 8(a) is plotted in Fig. 9(b). The period of fluctuation becomes $2\pi/\omega$ because $U_{\mathrm{Ising,T}}(\tau/2)$ instead of $U_{\mathrm{Ising,T}}(\tau)$ is involved. However, if the interaction in $H_{\mathrm{Ising,T}}$ can be turned off when H_{p0} is simulated, those fluctuations can be avoided, as shown in Fig. 10(a).

The fidelity of a simulation algorithm can be increased when tunable parameters of the simulator are increased, as exemplified in Fig. 10. The effect of tunable parameters is significant except for the simulator with the longitudinal Ising Hamiltonian, in which all terms commute with each other.

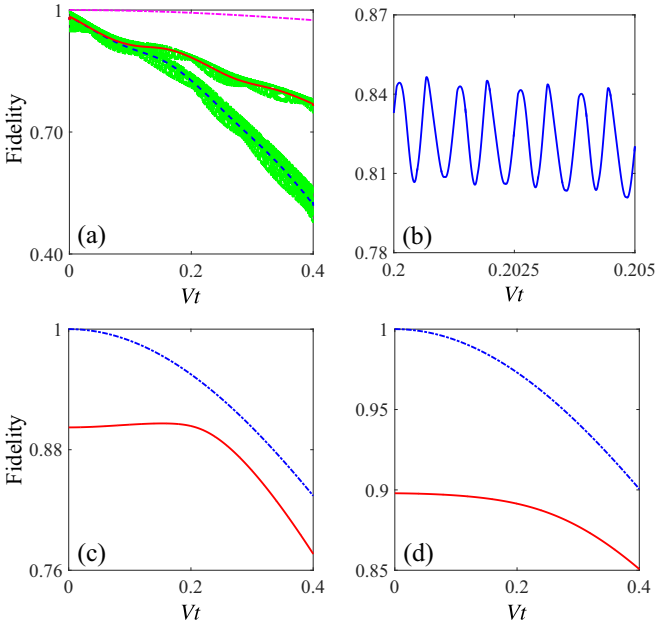

FIG. 10. Increase of simulation fidelity contributed by tunable parameters of four-qubit simulators containing (a) and (b) transverse Ising-type, (c) XY-type and (d) Heisenberg-type nearest-neighbor interactions. In all four panels, $\varepsilon_l = 2 \times 10^{12}$Hz, $\omega_l = 5 \times 10^9$Hz ($l = 1, \ldots, N$), $V_l = -2 \times 10^8$Hz. In (a) and (b), $J_l = 3 \times 10^7$Hz ($l = 1, \ldots, N-1$), and the whole simulation task is divided into $M = 20$ intervals; in (c) and (d) $J_l = 3 \times 10^6$Hz ($l = 1, \ldots, N-1$), and the whole simulation task is divided into $M = 10$ intervals. Furthermore, the subprocess in (c) and (d) for simulators with constant parameters to simulate $e^{\pm i\tau(\sigma_l^x\sigma_{l+1}^x+\sigma_l^y\sigma_{l+1}^y)\pi/4}$ ($l = 1, \ldots, N-1$) is divided into 200 intervals in order to reduce the error introduced by short-time approximation. In (a), the blue dashed curve stands for the average fidelity when all the parameters of the simulator are constant. The red solid curve stands for the average fidelity when only ω_l ($l = 1, \ldots, N$) are tunable. Green dotted curves stand for the high-frequency fluctuation of simulation fidelity originating from Eq. (33) associated with the above two cases. The magenta dash-dotted curve gives the fidelity when all the parameters of the simulator can be turned on and off during the simulation process. The detailed shape of the fidelity from a simulator with constant parameters over a short interval is shown in (b). In both (c) and (d), the red solid curve stands for the average fidelity when all the parameters of the simulator are constant, while the blue dash-dotted curve gives the fidelity when all the parameters of the simulator can be turned on and off.

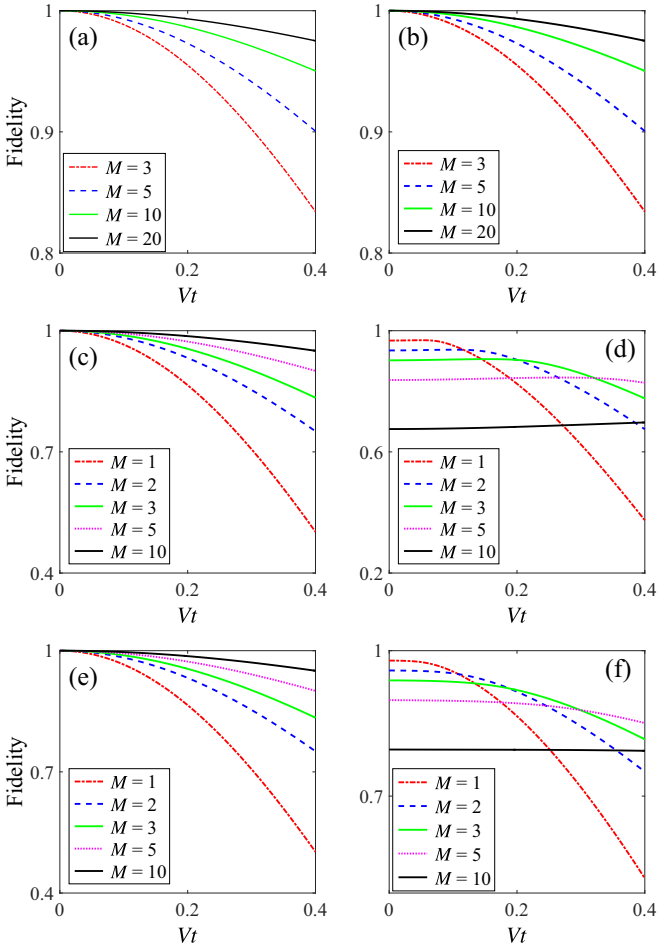

FIG. 11. Effect of changing the number of intervals M that the whole simulation process is divided into on the fidelity for four-qubit simulators containing (a) longitudinal Ising-type, (b) transverse Ising-type, (c) and (d) XY-type, and (e) and (f) Heisenberg-type nearest-neighbor interactions. In (c) and (e), all parameters of the simulators can be turned off and on during the process, while in (d) and (f) they are constant. In all six panels, $\varepsilon_l = 2 \times 10^{12}$Hz, $\omega_l = 5 \times 10^9$Hz ($l = 1, \ldots, N$), $V_l = -2 \times 10^8$Hz; in (a) and (b) $J_l = 3 \times 10^7$Hz, and in (c), (d), (e), and (f) $J_l = 1 \times 10^6$Hz. The subprocess in (d) and (f) for simulators with constant parameters to simulate $e^{\pm i(\sigma_l^x\sigma_{l+1}^x+\sigma_l^y\sigma_{l+1}^y)\pi/4}$ ($l = 1, \ldots, N-1$) is divided into $G = 200$ intervals in order to reduce the error introduced by short-time approximation. In (a) and (b), the curves from top to bottom correspond to $M = 20, 10, 5, 3$, respectively. In (c) and (e), the curves from top to bottom correspond to $M = 10, 5, 3, 2, 1$, respectively. In (d) and (f), the curves from bottom to top (counted from the leftmost side) correspond to $M = 10, 5, 3, 2, 1$, respectively.

The use of Trotter's formula with the short-time approximation improves the simulation fidelity significantly, as illustrated in Fig. 11. For simulators with longitudinal or transverse Ising interactions or tunable XY or Heisenberg interactions, we find that the larger the number of time intervals the total simulation time is divided into is, the higher the simulation fidelity obtained is, as in Figs. 11 (a), 11(b), 11(c), and 11(e). We believe that the error introduced by short-time approximation can be reduced in this way [78,79]. Nevertheless, for simulators with fixed-parameter XY or Heisenberg interaction Hamiltonians, we notice that the overall fidelity is sensitive to that of the subcircuit used to simulate $U_{l,l+1}^{xx+yy}[\pi/(4J_l)] = e^{\pm i\tau(\sigma_l^x\sigma_{l+1}^x+\sigma_l^y\sigma_{l+1}^y)\pi/4}$ ($l = 1, \ldots, N-1$) [see Figs. 11(d) and 11(f)]. On the other hand, in contrast to the error due to short-time approximation, the error from simulating $U_{l,l+1}^{xx+yy}[\pi/(4J_l)]$ increases with the running times of the subcircuit. Figures 11(d) and 11(f) show that when the simulation time is relatively short and the error from Trotter's formula is small, the overall simulation fidelity is mainly determined by that of simulating $U_{l,l+1}^{xx+yy}[\pi/(4J_l)]$. Therefore, we conclude that in this case the larger the number of time steps the total time for completing the whole task is divided into is, the longer $U_{l,l+1}^{xx+yy}[\pi/(4J_l)]$ simulation process is run, and the larger the error is. When the simulation time

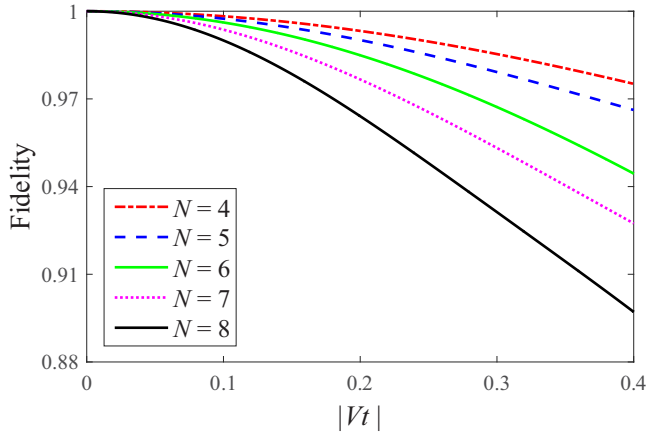

FIG. 12. Fidelity of the algorithm run by a quantum simulator with transverse Ising-type nearest-neighbor interactions containing different number of qubits. Every term in the Hamiltonian of the simulator can be turned on and off during the simulation process. $\varepsilon_l = 2 \times 10^{12}$Hz, $\omega_l = 5 \times 10^9$Hz ($l = 1, \ldots, N$), $V_l = -2 \times 10^8$Hz, $J_l = 3 \times 10^7$Hz ($l = 1, \ldots, N-1$). The whole simulation task is divided into $M = 20$ intervals. The curves from top to bottom correspond to $N = 4, 5, 6, 7, 8$, respectively.

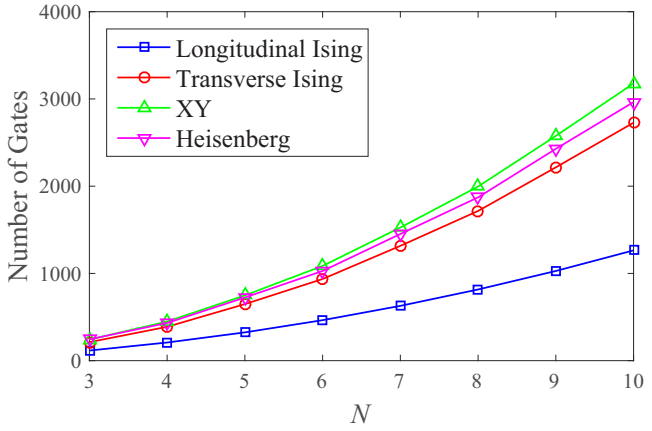

FIG. 13. Total number of external gates in the simulation process for four types of simulators with constant parameters. Here, the complexity is shown for a single running process, in which both the simulation task and subprocess to simulate $e^{\pm i(\sigma_l^x \sigma_{l+1}^x + \sigma_l^y \sigma_{l+1}^y)\pi/4}$ ($l = 1, \ldots, N-1$) are not further divided into any subintervals ($M = 1$, $G = 1$).

becomes longer, the error from Trotter's formula becomes dominant. Therefore, as shown in Figs. 11(d) and 11(f), all curves are almost flat at the short simulation time and drop when the time increases. Moreover, the fidelity of the simulation with a smaller number M of intervals is higher for a shorter simulation time but lower for a longer simulation time.

Figure 12 suggests that if other conditions are the same, the fidelity of simulation algorithms decreases when the qubit number in quantum simulators is increased. In practice, this error can be compensated by reducing the error due to the short-time approximation.

V. COMPLEXITY ANALYSIS

Let us now analyze the complexity of the algorithms, which is determined by the total number of external single-qubit logic gates required for the simulation process. We will show that the algorithms are polynomial.

The number of single-qubit gates in any of the quantum circuits in the previous sections increases linearly with the number of qubits N in the simulator. One can extract $U_l^z(\tau) = \exp(-i\tau\omega_l\sigma_l^z/2)$ in the complexity $O(N)$. The simulation of individual $e^{-itH_{p0}} = \bigotimes_{m=1}^N U_m^z(\varepsilon_m t/\omega_m)$ requires $O(N^2)$ external gates. We find that $U_{l,l+1}^{zz}(\tau) = \exp(-i\tau J_l \sigma_l^z \sigma_{l+1}^z)$ or $U_{l,l+1}^{xx+yy} = \exp[-i\tau J_l(\sigma_l^x\sigma_{l+1}^x + \sigma_l^y\sigma_{l+1}^y)]$ can also be simulated within $O(N)$. As shown in [40], it can be shown that

$$e^{i\frac{\pi}{2}X_{l,l+1}} U_{m,l}^{zz}(\tau) e^{-i\frac{\pi}{2}X_{l,l+1}} = U_{m,l+1}^{zz}(\tau) \tag{34}$$

for $m < l$, where $X_{l,m} = (\sigma_l^x\sigma_m^x + \sigma_l^y\sigma_m^y)/2$. Thus, it needs $O(N^2)$ to simulate an arbitrary long-range interaction $U_{m,l}^{zz}(\tau)$. Since $N(N+1)/2$ terms are included in the pairing Hamiltonian (6), simulation of all these interactions requires $O(N^4)$ logic gates, or the complexity of the whole algorithm is $O(N^4)$.

In Fig. 13, we calculate total numbers of external gates for four types of simulators with all constant parameters when $N \leqslant 10$. It shows that the longitudinal Ising simulator has the lowest complexity. On the other hand, if the parameters of the simulators are tunable, the complexity is significantly reduced when the scale of the simulator increases, as shown in Fig. 14.

Furthermore, although higher simulation fidelity can be obtained through the short-time approximation by dividing the simulation process into $M > 1$ intervals, this is at the expense of higher complexity since the number of logic gates is M times of the gate number without the short-time approximation. Moreover, although Trotter's formula can be applied to the subprocess of simulating $\exp[\pm i\pi(\sigma_l^x\sigma_{l+1}^x + \sigma_l^y\sigma_{l+1}^y)/4]$ ($l = 1, \ldots, N-1$), the complexity grows linearly with the number G of intervals that this subprocess is divided into, which is shown in Fig. 15. We can also find that if simulators with

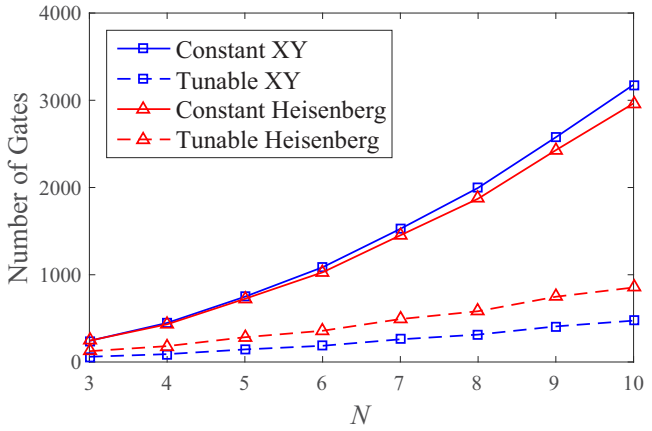

FIG. 14. Effects of tunable parameters on the complexity for XY-type and Heisenberg-type simulators. Points on solid lines stand for the case when all parameters in the simulator are constant, while points on dashed lines give the result when they are all tunable. Here, the total number of external gates is shown for a single running process, in which both the simulation task and subprocess to simulate $e^{\pm i(\sigma_l^x\sigma_{l+1}^x + \sigma_l^y\sigma_{l+1}^y)\pi/4}$ ($l = 1, \ldots, N-1$) are not further divided into any subintervals ($M = 1, G = 1$).

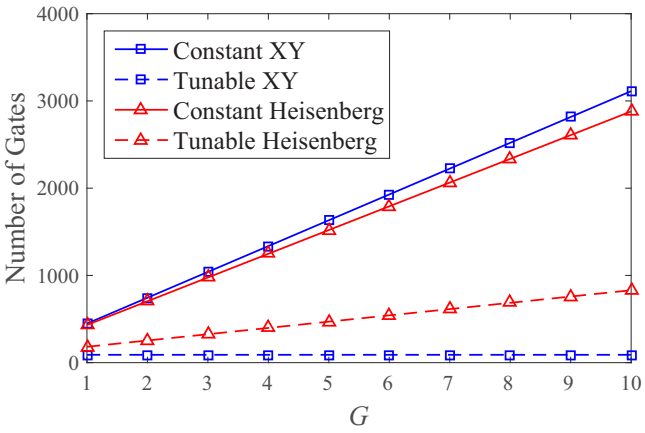

FIG. 15. Increasing of complexity due to the processes for simulating $e^{\pm i(\sigma_l^x\sigma_{l+1}^x+\sigma_l^y\sigma_{l+1}^y)\pi/4}$ $(l=1,\ldots,N-1)$ being divided into more subintervals. XY and Heisenberg simulators are taken as the examples. Points on solid lines stand for the case when all parameters in the simulator are constant, while points on dashed lines give the result when they are all tunable. Here, the whole simulation task is not further divided into any subintervals ($M=1$).

tunable parameters are available, the effect of G on the total number of external gates will be reduced. In particular, when all parameters of an XY-type simulator are tunable, the growth of G has no effect on the simulation complexity.

VI. MEASUREMENT SCHEME

Now we come to the measurement or readout approach as the last step of our simulation algorithm. Based on a quantum phase estimation algorithm [80], the measurement circuit is shown in Fig. 16. We use an ancillary qubit, denoted by a red 0 and entangled with the simulator. We measure the ancilla at the end of the simulation process. We use one qubit, marked by a red 1, to directly interact with the ancillary qubit in the whole simulator. $|\pm\rangle_0=(|\uparrow\rangle_0\pm|\downarrow\rangle_0)/\sqrt{2}$ are eigenstates of operator σ_x^0 for the ancillary qubit.

The readout processes are as follows. First, the ancillary qubit is prepared for the state $|+\rangle_0$, while the simulator, including qubits 1 to N involved in the algorithms, is prepared for a state $|\psi\rangle$. The whole system is initially at $|\Psi_0\rangle=|+\rangle_0\otimes|\psi\rangle$. We then apply a controlled-NOT gate denoted by $\mathrm{CNOT}_{0\to1}$ to qubit 0 and qubit 1 so that the system state becomes $|\Psi_1\rangle=\mathrm{CNOT}_{0\to1}|\Psi_0\rangle$, where the ancilla serves as the control qubit and qubit 1 serves as the target qubit. We run the complete simulation algorithms for a time interval t, represented by $U_p(t)=e^{-itH_p}$, such that the system becomes $|\Psi_2\rangle=[I_0\otimes U_p(t)]|\Psi_1\rangle$. A new controlled-NOT gate is applied to qubit 0 and qubit 1 again, where the ancilla again serves as the control qubit and qubit 1 serves as the target qubit. The state of the whole system ends up as $|\Psi_3\rangle=\mathrm{CNOT}_{0\to1}|\Psi_2\rangle$. Finally, the ancilla is measured on the $\{|+\rangle_0,|-\rangle_0\}$ basis. The probabilities of obtaining the states $|\pm\rangle$ are $P_0^{\pm}(t)$, respectively, which vary with time t. We can use either $P_0^+(t)$ or $P_0^-(t)$ to extract the spectrum information of the simulator. For example, $P_0^+(t)$ is calculated as

$$P_0^+(t)=\tfrac{1}{2}+\tfrac{1}{4}\big[\langle\psi|\sigma_1^x(t)\sigma_1^x(0)|\psi\rangle+\text{c.c.}\big], \tag{35}$$

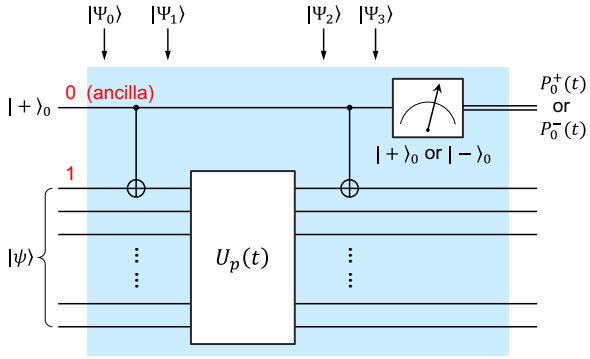

FIG. 16. Measurement scheme for the simulation algorithms in order to extract information such as the energy spectrum from the simulator. $|+\rangle_0$ and $|\psi\rangle$ stand for the initial state of the ancillary qubit and the quantum simulator, respectively. Indexes 0 and 1 denote the ancilla and the single qubit in the simulator directly coupled with the ancilla, respectively. $|\Psi_0\rangle$, $|\Psi_1\rangle$, $|\Psi_2\rangle$, and $|\Psi_3\rangle$ are the states of the whole system during the simulation process. $U_p(t)$ is the time-evolution operator including the complete simulation algorithms, which is explicitly equivalent to the pairing Hamiltonian. Two CNOT gates in which qubit 0 (ancilla) serves as the control qubit and qubit 1 serves as the target qubit are graphically shown. Measurement is done for the ancilla on the $|+\rangle_0$ or $|-\rangle_0$ basis, giving probability $P_0^+(t)$ or $P_0^-(t)$ as the result, respectively, where t corresponds to the evolution time for the BCS system in $U_p(t)$.

where $\sigma_1^x(t)=U_p^\dagger(t)\sigma_1^xU_p(t)$ is in the Heisenberg picture.

We could now expand the initial state with a complete set of quantum numbers n, i, and β_i, $|\psi\rangle=\sum_{n,i,\beta_i}B_{n,i,\beta_i}|n,i,\beta_i\rangle$. Here, n is the total number of spin-up qubits in our simulator. i denotes the energy level $E_{n,i}$ with a given n, and β_i denotes the degeneracy for a given energy level $E_{n,i}$. Physically, n is also the number of Cooper pairs in the simulated pairing Hamiltonian. States with different quantum numbers n are mutually orthogonal, $\langle m,j,\beta_j|n,i,\beta_i\rangle=\delta_{nm}\langle m,j,\beta_j|n,i,\beta_i\rangle$. In order to simplify the calculation, we can especially prepare qubit 1 in the spin-up state, such that $\sigma_1^z|\psi\rangle=|\psi\rangle$ and

$$\langle\psi|\sigma_1^x(t)\sigma_1^x(0)|\psi\rangle=\sum_{n,i,j}\tilde{C}_{n,i,j}e^{it(E_{n,j}-E_{n-1,i})}, \tag{36}$$

where $\tilde{C}_{n,i,j}=\sum_{\beta_i,\beta_j}B^*_{n,j,\beta_j}B_{n,i,\beta_i}\langle n,j,\beta_j|n,i,\beta_i\rangle$. To study the measurement result in the frequency domain, we can take the Fourier transform $\tilde{\rho}_0^+(\omega)$ of $P_0^+(t)$,

$$\begin{aligned}\tilde{\rho}_0^+(\omega)&=\pi\delta(\omega)\\&\quad+\frac{\pi}{2}\sum_{n,i,j}\tilde{C}_{n,i,j}\delta(\omega+E_{n,j}-E_{n-1,i})\\&\quad+\frac{\pi}{2}\sum_{n,i,j}\tilde{C}^*_{n,i,j}\delta(\omega-E_{n,j}+E_{n-1,i}).\end{aligned} \tag{37}$$

The spectrum of $P_0^+(t)$ is symmetric on amplitude and antisymmetric on phase because $P_0^+(t)$ is real. In the amplitude spectrum, there should be sharp peaks, ideally, δ-shaped peaks at frequencies $\omega^{\pm}_{n,i,j}=\pm(E_{n,j}-E_{n-1,i})$. The energy spectra of the pairing Hamiltonian could be extracted from these frequencies. For instance, the energy gap between the ground state and the first excitation state with n-Cooper pairs can be

obtained by

$$2\Delta_n = E_{n,1} - E_{n,0} = \left(E_{n,1} - E_{n-1,i}\right) - \left(E_{n,0} - E_{n-1,i}\right) = \omega^{+}_{n,i,1} - \omega^{+}_{n,i,0}. \tag{38}$$

Generally, the low-lying energy spectra of a pairing Hamiltonian are of great interest. Using the adiabatic method developed in Ref. [40], we can prepare initial states that involve a few eigenstates of the simulated pairing Hamiltonian to improve the efficiency of our measurement approach.

VII. CONCLUSION

In summary, based on the quantum simulation algorithm for the paring Hamiltonians using NMR systems, we have studied a set of algorithms to simulate the pairing Hamiltonians using four representative nearest-neighbor interactions, e.g., the longitudinal Ising Hamiltonian, transverse Ising Hamiltonian, XY Hamiltonian, and Heisenberg Hamiltonian, which extensively exist in various solid-state quantum computing systems. We find the following: (i) The fidelity of a simulation algorithm can be increased when the number of tunable parameters of the simulator is increased. (ii) If other conditions are the same, the fidelity of the simulation algorithm decreases with increasing qubit number in the quantum simulator. (iii) For simulators with longitudinal Ising interactions, transverse Ising interactions, tunable XY interactions, or Heisenberg interactions, higher fidelity, using Trotter's formula with the short-time approximation, can be obtained if the total simulation time is divided into more time intervals. (iv) The algorithm complexity of the longitudinal Ising simulator is lowest for all four interaction Hamiltonians with constant interaction strengths. (v) More controllable parameters in a given quantum simulator correspond to lower complexity of the algorithms.

Our study establishes a link between solid-state quantum computing models and outstanding many-body problems in finite-system quantum physics. We know that solving the pairing Hamiltonian is a crucial issue in solving quantum many-body problems in BCS models, nuclear physics, and other many-body systems. Thus, our algorithms provide not only a necessary complement to the NMR algorithm but also new ways to simulate quantum many-body problems. Since the four types of nearest-neighbor interaction Hamiltonians are shared by various quantum systems [72,73,76], our algorithms can, in principle, be applied to various solid-state systems. We would also like to point out that superconducting quantum computing with more than ten qubits is experimentally realizable now [81]. The controllability, gate fidelity, and decoherence of superconducting quantum circuits are more advanced than other solid-state quantum devices. Moreover, superconducting quantum circuits can be used to engineer all four types of interaction Hamiltonians; thus, our algorithm might be easier to realize with superconducting quantum circuits in the near future.

ACKNOWLEDGMENTS

This work is supported by the National Basic Research Program (973) of China, Grant No. 2014CB921401.

APPENDIX

In this appendix we show the derivation of Eq. (8),

$$U^{z}_{l}(\tau) = \left(\bigotimes_{j''\neq l} e^{i\frac{\pi}{2}\sigma^{x}_{j''}}\right) U_{\mathrm{Ising,L}}\left(\frac{\tau}{4}\right)\left(\bigotimes_{j'} e^{i\frac{\pi}{2}\sigma^{x}_{j'}}\right) U_{\mathrm{Ising,L}}\left(\frac{\tau}{4}\right) \times \left(\bigotimes_{j''\neq l} e^{-i\frac{\pi}{2}\sigma^{x}_{j''}}\right) U_{\mathrm{Ising,L}}\left(\frac{\tau}{4}\right)\left(\bigotimes_{j'} e^{-i\frac{\pi}{2}\sigma^{x}_{j'}}\right) U_{\mathrm{Ising,L}}\left(\frac{\tau}{4}\right), \tag{A1}$$

in detail.

Recall the time-evolution operator for quantum simulators with longitudinal Ising-type nearest-neighbor interaction

$$U_{\mathrm{Ising,L}}(\tau) = \exp\left[-i\tau\left(\sum_{l=1}^{N}\frac{\omega_l}{2}\sigma^{z}_{l} + \sum_{l=1}^{N-1} J_l\sigma^{z}_{l}\sigma^{z}_{l+1}\right)\right] = \exp\left(-i\tau\sum_{l=1}^{N}\frac{\omega_l}{2}\sigma^{z}_{l}\right)\exp\left(-i\tau\sum_{l=1}^{N-1} J_l\sigma^{z}_{l}\sigma^{z}_{l+1}\right). \tag{A2}$$

According to the Baker-Hausdorff formula,

$$e^{i\lambda G}Ae^{-i\lambda G} = A + i\lambda[G,A] + \tfrac{(i\lambda)^2}{2!}[G,[G,A]] + \cdots + \tfrac{(i\lambda)^n}{n!}\underbrace{[G,\ldots[G,A]\ldots]}_{n\ \text{commutators}} + \cdots, \tag{A3}$$

when $\lambda = \varphi, G = \sigma^{x}_{m}, A = \sigma^{z}_{m}$, it can be verified that

$$e^{i\varphi\sigma^{x}_{m}}\sigma^{z}_{m}e^{-i\varphi\sigma^{x}_{m}} = \cos(2\varphi)\sigma^{z}_{m} + \sin(2\varphi)\sigma^{y}_{m} \tag{A4}$$

Taking $\varphi = \pm\pi/2$, we have

$$e^{\pm i\frac{\pi}{2}\sigma^{x}_{m}}\sigma^{z}_{m}e^{\mp i\frac{\pi}{2}\sigma^{x}_{m}} = -\sigma^{z}_{m}. \tag{A5}$$

Therefore,

$$\left(\bigotimes_{j''\neq l} e^{i\frac{\pi}{2}\sigma^x_{j''\neq l}}\right) U_{\mathrm{Ising,L}}\left(\frac{\tau}{4}\right)\left(\bigotimes_{j'} e^{i\frac{\pi}{2}\sigma^x_{j'}}\right) U_{\mathrm{Ising,L}}\left(\frac{\tau}{4}\right)\left(\bigotimes_{j''} e^{-i\frac{\pi}{2}\sigma^x_{j''}}\right) U_{\mathrm{Ising,L}}\left(\frac{\tau}{4}\right)\left(\bigotimes_{j'} e^{-i\frac{\pi}{2}\sigma^x_{j'}}\right) U_{\mathrm{Ising,L}}\left(\frac{\tau}{4}\right)$$

$$\begin{aligned}
&= e^{-i\frac{\tau}{4}(\omega_l\sigma_l^z/2+\sum_{j'}\omega_{j'}\sigma_{j'}^z/2-\sum_{j''\neq l}\omega_{j''}\sigma_{j''}^z/2)} e^{-i\frac{\tau}{4}\left(J_{l-1}\sigma_{l-1}^z\sigma_l^z+J_l\sigma_l^z\sigma_{l+1}^z-\sum_{j\neq l-1,l}^{N-1}J_j\sigma_j^z\sigma_{j+1}^z\right)}\\
&\quad\times e^{-i\frac{\tau}{4}(\omega_l\sigma_l^z/2-\sum_{j'}\omega_{j'}\sigma_{j'}^z/2-\sum_{j''\neq l}\omega_{j''}\sigma_{j''}^z/2)} e^{-i\frac{\tau}{4}\left(-J_{l-1}\sigma_{l-1}^z\sigma_l^z-J_l\sigma_l^z\sigma_{l+1}^z+\sum_{j\neq l-1,l}^{N-1}J_j\sigma_j^z\sigma_{j+1}^z\right)}\\
&\quad\times e^{-i\frac{\tau}{4}(\omega_l\sigma_l^z/2-\sum_{j'}\omega_{j'}\sigma_{j'}^z/2+\sum_{j''\neq l}\omega_{j''}\sigma_{j''}^z/2)} e^{-i\frac{\tau}{4}\left(-J_{l-1}\sigma_{l-1}^z\sigma_l^z-J_l\sigma_l^z\sigma_{l+1}^z-\sum_{j\neq l-1,l}^{N-1}J_j\sigma_j^z\sigma_{j+1}^z\right)}\\
&\quad\times e^{-i\frac{\tau}{4}(\omega_l\sigma_l^z/2+\sum_{j'}\omega_{j'}\sigma_{j'}^z/2+\sum_{j''\neq l}\omega_{j''}\sigma_{j''}^z/2)} e^{-i\frac{\tau}{4}(J_{l-1}\sigma_{l-1}^z\sigma_l^z+J_l\sigma_l^z\sigma_{l+1}^z+\sum_{j\neq l-1,l}^{N-1}J_j\sigma_j^z\sigma_{j+1}^z)}\\
&= e^{-i\tau\omega_l\sigma_l^z/2} = U_l^z(\tau). \qquad \text{(A6)}
\end{aligned}$$

Here, j' is an even (odd) number, and j'' is an odd (even) number if l is an odd (even) number, where $j''\neq l$. j goes over all qubit indices.

[1] I. Buluta and F. Nori, Science **326**, 108 (2009).
[2] I. M. Georgescu, S. Ashhab, and F. Nori, Rev. Mod. Phys. **86**, 153 (2014).
[3] A. Trabesinger, Nat. Phys. **8**, 263 (2012).
[4] J. I. Cirac and P. Zoller, Nat. Phys. **8**, 264 (2012).
[5] R. Feynman, Int. J. Theor. Phys. **21**, 467 (1982).
[6] S. Lloyd, Science **273**, 1073 (1996).
[7] J. Simon, W. S. Bakr, R. Ma, M. E. Tai, P. M. Preiss, and M. Greiner, Nature (London) **472**, 307 (2011).
[8] B. P. Lanyon, C. Hempel, D. Nigg, M. Müller, R. Gerritsma, F. Zähringer, P. Schindler, J. T. Barreiro, M. Rambach, G. Kirchmair, M. Hennrich, P. Zoller, R. Blatt, and C. F. Roos, Science **334**, 57 (2011).
[9] D. Jaksch and P. Zoller, Ann. Phys. (N.Y.) **315**, 52 (2005).
[10] M. Lewenstein, A. Sanpera, V. Ahufinger, B. Damski, A. Sen(De), and U. Sen, Adv. Phys. **56**, 243 (2007).
[11] C. Schneider, D. Porras, and T. Schaetz, Rep. Prog. Phys. **75**, 024401 (2012).
[12] I. Kassal, J. D. Whitfield, A. Perdomo-Ortiz, M.-H. Yung, and A. Aspuru-Guzik, Annu. Rev. Phys. Chem. **62**, 185 (2011).
[13] D. Lu, B. Xu, N. Xu, Z. Li, H. Chen, X. Peng, R. Xu, and J. Du, Phys. Chem. Chem. Phys. **14**, 9411 (2012).
[14] I. Bloch, J. Dalibard, and S. Nascimbène, Nat. Phys. **8**, 267 (2012).
[15] R. Blatt and C. F. Roos, Nat. Phys. **8**, 277 (2012).
[16] A. Aspuru-Guzik and P. Walther, Nat. Phys. **8**, 285 (2012).
[17] A. A. Houck, H. E. Türeci, and J. Koch, Nat. Phys. **8**, 292 (2012).
[18] J. W. Britton, B. C. Sawyer, A. C. Keith, C.-C. J. Wang, J. K. Freericks, H. Uys, M. J. Biercuk, and J. J. Bollinger, Nature (London) **484**, 489 (2012).
[19] T. Byrnes and Y. Yamamoto, Phys. Rev. A **73**, 022328 (2006).
[20] R. Gerritsma, G. Kirchmair, F. Zähringer, E. Solano, R. Blatt, and C. F. Roos, Nature (London) **463**, 68 (2010).
[21] P. M. Alsing, J. P. Dowling, and G. J. Milburn, Phys. Rev. Lett. **94**, 220401 (2005).
[22] P. D. Nation, J. R. Johansson, M. P. Blencowe, and F. Nori, Rev. Mod. Phys. **84**, 1 (2012).
[23] B. P. Lanyon, J. D. Whitfield, G. G. Gillett, M. E. Goggin, M. P. Almeida, I. Kassal, J. D. Biamonte, M. Mohseni, B. J. Powell, M. Barbieri, A. Aspuru-Guzik, and A. G. White, Nat. Chem. **2**, 106 (2010).
[24] M.-H. Yung, J. Casanova, A. Mezzacapo, J. McClean, L. Lamata, A. Aspuru-Guzik, and E. Solano, Sci. Rep. **4**, 3589 (2014).
[25] C. Monroe and J. Kim, Science **339**, 1164 (2013).
[26] D. D. Awschalom, L. C. Bassett, A. S. Dzurak, E. L. Hu, and J. Petta, Science **339**, 1174 (2013).
[27] R. Blatt and D. Wineland, Nature (London) **453**, 1008 (2008).
[28] I. Bloch, Nature (London) **453**, 1016 (2008).
[29] R. Hanson and D. D. Awschalom, Nature (London) **453**, 1043 (2008).
[30] S. Raeisi, N. Wiebe, and B. C. Sanders, New J. Phys. **14**, 103017 (2012).
[31] N. Wiebe, D. W. Berry, P. Hoyer, and B. C. Sanders, J. Phys. A **44**, 445308 (2011).
[32] Z.-X. Chen, Z.-W. Zhou, X. Zhou, X.-F. Zhou, and G.-C. Guo, Phys. Rev. A **81**, 022303 (2010).
[33] M.-X. Huo, C. Noh, B. M. Rodríguez-Lara, and D. G. Angelakis, Phys. Rev. A **86**, 043840 (2012).
[34] M. Di Liberto, C. E. Creffield, G. I. Japaridze, and C. Morais Smith, Phys. Rev. A **89**, 013624 (2014).
[35] J. Casanova, A. Mezzacapo, L. Lamata, and E. Solano, Phys. Rev. Lett. **108**, 190502 (2012).
[36] A. Mezzacapo, J. Casanova, L. Lamata, and E. Solano, Phys. Rev. Lett. **109**, 200501 (2012).
[37] J. T. Barreiro, M. Müller, P. Schindler, D. Nigg, T. Monz, M. Chwalla, M. Hennrich, C. F. Roos, P. Zoller, and R. Blatt, Nature (London) **470**, 486 (2011).
[38] K. Kim, M.-S. Chang, S. Korenblit, R. Islam, E. E. Edwards, J. K. Freericks, G.-D. Lin, L.-M. Duan, and C. Monroe, Nature (London) **465**, 590 (2010).
[39] J. Struck, C. Ölschläger, R. Le Targat, P. Soltan-Panahi, A. Eckardt, M. Lewenstein, P. Windpassinger, and K. Sengstock, Science **333**, 996 (2011).
[40] L.-A. Wu, M. S. Byrd, and D. A. Lidar, Phys. Rev. Lett. **89**, 057904 (2002).
[41] K. R. Brown, R. J. Clark, and I. L. Chuang, Phys. Rev. Lett. **97**, 050504 (2006).
[42] X. Yang, A. M. Wang, F. Xu, and J. Du, Chem. Phys. Lett. **422**, 20 (2006).
[43] J. Du, N. Xu, X. Peng, P. Wang, S. Wu, and D. Lu, Phys. Rev. Lett. **104**, 030502 (2010).

[44] J. Zhang, T.-C. Wei, and R. Laflamme, Phys. Rev. Lett. **107**, 010501 (2011).
[45] T. D. Ladd, F. Jelezko, R. Laflamm, Y. Nakamura, C. Monroe, and J. L. O'Brien, Nature (London) **464**, 45 (2010).
[46] M. H. Devoret and R. J. Schoelkopf, Science **339**, 1169 (2013).
[47] J. Clarke and F. K. Wilhelm, Nature (London) **453**, 1031 (2008).
[48] J. Q. You and F. Nori, Phys. Today **58**(11), 42 (2005).
[49] J. Q. You and F. Nori, Nature (London) **474**, 589 (2011).
[50] R. Barends *et al.*, Nature (London) **508**, 500 (2014).
[51] D. L. Underwood, W. E. Shanks, J. Koch, and A. A. Houck, Phys. Rev. A **86**, 023837 (2012).
[52] P. Roushan *et al.*, Nature (London) **515**, 241 (2014).
[53] D. Marcos, P. Rabl, E. Rico, and P. Zoller, Phys. Rev. Lett. **111**, 110504 (2013).
[54] U. Las Heras, A. Mezzacapo, L. Lamata, S. Filipp, A. Wallraff, and E. Solano, Phys. Rev. Lett. **112**, 200501 (2014).
[55] T. Mao and Z. D. Wang, Phys. Rev. A **91**, 012336 (2015).
[56] J. Ghosh and B. C. Sanders, New J. Phys. **18**, 033015 (2016).
[57] M. A. Eriksson, S. N. Coppersmith, and M. G. Lagally, MRS Bull. **38**, 794 (2013).
[58] L. Gordon, J. R. Weber, J. B. Varley, A. Janotti, D. D. Awschalom, and C. G. Van de Walle, MRS Bull. **38**, 802 (2013).
[59] T. Yamamoto, Y. Pashkin, O. Astafiev, Y. Nakamura, and J. S. Tsai, Nature (Lonodn) **425**, 941 (2003).
[60] J. B. Majer, F. G. Paauw, A. C. J. ter Haar, C. J. P. M. Harmans, and J. E. Mooij, Phys. Rev. Lett. **94**, 090501 (2005).
[61] J. Siewert, R. Fazio, G. M. Palma, and E. Sciacca, J. Low Temp. Phys. **118**, 795 (2000).
[62] N. Schuch and J. Siewert, Phys. Rev. A **67**, 032301 (2003).
[63] T. P. Orlando, J. E. Mooij, L. Tian, C. H. van der Wal, L. S. Levitov, S. Lloyd, and J. J. Mazo, Phys. Rev. B **60**, 15398 (1999).
[64] Y. Makhlin, G. Schön, and A. Shnirman, Nature (London) **398**, 305 (1999).
[65] J. Q. You, J. S. Tsai, and F. Nori, Phys. Rev. Lett. **89**, 197902 (2002).
[66] Y. A. Pashkin, T. Yamamoto, O. Astafiev, Y. Nakamura, D. V. Averin, and J. S. Tsai, Nature (London) **421**, 823 (2003).
[67] R. McDermott, R. W. Simmonds, M. Steffen, K. B. Cooper, K. Cicak, K. D. Osborn, S. Oh, D. P. Pappas, and J. M. Martinis, Science **307**, 1299 (2005).
[68] P. Bertet, C. J. P. M. Harmans, and J. E. Mooij, Phys. Rev. B **73**, 064512 (2006).
[69] A. Imamoglu, D. D. Awschalom, G. Burkard, D. P. DiVincenzo, D. Loss, M. Sherwin, and A. Small, Phys. Rev. Lett. **83**, 4204 (1999).
[70] D. Mozyrsky, V. Privman, and M. L. Glasser, Phys. Rev. Lett. **86**, 5112 (2001).
[71] L. Quiroga and N. F. Johnson, Phys. Rev. Lett. **83**, 2270 (1999).
[72] D. Loss and D. P. DiVincenzo, Phys. Rev. A **57**, 120 (1998).
[73] B. Kane, Nature (London) **393**, 133 (1998).
[74] G. Burkard, D. Loss, and D. P. DiVincenzo, Phys. Rev. B **59**, 2070 (1999).
[75] X. Hu and S. Das Sarma, Phys. Rev. A **61**, 062301 (2000).
[76] R. Vrijen, E. Yablonovitch, K. Wang, H. W. Jiang, A. Balandin, V. Roychowdhury, T. Mor, and D. DiVincenzo, Phys. Rev. A **62**, 012306 (2000).
[77] D. W. Leung, I. L. Chuang, F. Yamaguchi, and Y. Yamamoto, Phys. Rev. A **61**, 042310 (2000).
[78] H. F. Trotter, Proc. Am. Math. Soc. **10**, 545 (1959).
[79] M. A. Nielsen and I. L. Chuang, *Quantum Computation and Quantum Information* (Cambridge University Press, Cambridge, 2000).
[80] A. Y. Kitaev, arXiv:quant-ph/9511026.
[81] R. Barends *et al.*, Nat. Commun. **6**, 7654 (2015).